mathematics

MDPI

Article

Computational Analysis on Magnetized and Non-Magnetized Boundary Layer Flow of Casson Fluid Past a Cylindrical Surface by Using Artificial Neural Networking

Khalil Ur Rehman [1,2,*], Wasfi Shatanawi [1,3] and Andaç Batur Çolak [4]

[1] Department of Mathematics and Sciences, College of Humanities and Sciences, Prince Sultan University, Riyadh 11586, Saudi Arabia
[2] Department of Mathematics, Air University, PAF Complex E-9, Islamabad 44000, Pakistan
[3] Department of Mathematics, Faculty of Science, The Hashemite University, P.O. Box 330127, Zarqa 13133, Jordan
[4] Information Technologies Application and Research Center, Istanbul Commerce University, Istanbul 34445, Turkey
* Correspondence: kurrehman@psu.edu.sa

Abstract: In this article, we constructed an artificial neural networking model for the stagnation point flow of Casson fluid towards an inclined stretching cylindrical surface. The Levenberg–Marquardt training technique is used in multilayer perceptron network models. Tan–Sig and purelin transfer functions are carried in the layers. For better novelty, heat and mass transfer aspects are taken into account. The viscous dissipation, thermal radiations, variable thermal conductivity, and heat generation effects are considered by way of an energy equation while the chemical reaction effect is calculated by use of the concentration equation. The flow is mathematically modelled for magnetic and non-magnetic flow fields. The flow equations are solved by the shooting method and the outcomes are concluded by means of line graphs and tables. The skin friction coefficient is evaluated at the cylindrical surface for two different flow regimes and the corresponding artificial neural networking estimations are presented. The coefficient of determination values' proximity to one and the low mean squared error values demonstrate that each artificial neural networking model predicts the skin friction coefficient with high accuracy.

Keywords: Casson fluid; mixed convection; thermal radiations; shooting method; artificial neural networking; Levenberg–Marquardt technique

MSC: 76R10; 76-10; 65K05

Citation: Rehman, K.U.; Shatanawi, W.; Çolak, A.B. Computational Analysis on Magnetized and Non-Magnetized Boundary Layer Flow of Casson Fluid Past a Cylindrical Surface by Using Artificial Neural Networking. *Mathematics* **2023**, *11*, 326. https://doi.org/10.3390/math11020326

Academic Editor: Ramoshweu Solomon Lebelo

Received: 28 October 2022
Revised: 3 January 2023
Accepted: 4 January 2023
Published: 8 January 2023

1. Introduction

Alfven [1] was the pioneer of the field of magnetohydrodynamics (MHD) and since the study of MHD is still a subject that researchers are quite interested in Due to its extensive applications in daily life, for example blood flow control during surgery, magnetic endoscopy, cell separation, magnetic devices, tumor treatment, and drug targeting to mention just a few. Collectively, MHD plays a key role in industrial and biomedical sciences [2]. Owing to such importance, various recent studies performed by researchers such as Mustafa [3] have studied magnetized viscous flow by way of nonlinear surfaces. It has been demonstrated that temperature and flow fields have a straightforward analytical expression. He offered precise formulations for wall shear stress. He concludes that strong magnetic fields thin both the momentum and temperature layers. Additionally, as opposed to lower branches, upper branch solutions were more thoroughly chilled, resulting in increased heat transfer rates. The magnetized fluid by way of a porous channel with a radiation assumption was investigated by Akinbowale [4]. Heat and mass transfer are examined in relation to important rheological parameters such as the magnetic and pressure

gradient, the radiation parameter, and Prandtl and Reynolds numbers. It was found that increasing the pressure results in an increase in velocity, with the greatest effect occurring toward the center of the flow channel, whereas increasing the radiation parameter causes the temperature distribution to decrease, with the greatest effect occurring toward the electrically conducting wall. Hanumesh et al. [5] studied MHD peristaltic flow through an asymmetric tapered tube. Through a porous material, fluid with varied transport characteristics is transported. A low Reynolds number and a long wavelength were the fundamental assumptions used to formulate the problem. The momentum and energy equations' solutions were obtained using the perturbation method. The graphed answers show that a key factor in controlling the fluid velocity in the channel's center is the varying viscosity. The MHD fluid caused by an unstable stretched sheet with an expanded heat flux was into consideration by Ahmed et al. [6]. It was presumed that thermal conductivity and viscosity would change with the temperature. The flow equations were solved by an efficient shooting method and the Runge–Kutta algorithm. Graphical representations and in-depth analysis were carried out to examine the flow field. Liaqat et al. [7] studied heat transfer using self-propelled bioconvective microorganisms submerged in a water-based MHD nanofluid that included Cattaneo–Christov characteristics. Through Matlab programming, a finite element method was used to establish the numerical outcomes of the collection of non-linear equations. An important finding was that the density of the liquid was enhanced toward the melting factor. MHD micropolar tangent hyperbolic fluid flow toward the stretched surface was investigated by Pardeep et al. [8]. The collection of partial differential equations was transformed using similarity transformations to obtain the theoretically specified ordinary differential system. The issue was mathematically resolved using the bvp4c method. The major goal of this extensive investigation was to enhance heat transformation under the influence of numerous parameters. A number of physical factors were used to depict the heat transfer, skin friction, temperature, and velocity. It was discovered that changes in velocity and temperature profiles drove changes in the parameters that affected the size of the nanoparticles and the rate of heat transfer.

The Casson fluid model [9] has received a lot of attention from researchers due to its unique characteristics. Compared to conventional viscoplastic models, the Casson fluid model more closely matches rheological data for a variety of materials. Casson fluid, a shear-thinning fluid, is predicted to have a yield stress below which there is no flow, an infinite viscosity at a zero shear rate, and zero viscosity at an infinite shear rate. Casson fluids include intense fruit liquids, tomato sauce, soup, honey, and jellies. Furthermore, it is an approximate rheological model for chocolate and blood. Additionally, Casson fluid exhibits yield stress and is crucial in the biomechanics and polymer processing sectors. Owing to such importance, various researchers have considered the examination of the Casson flow field in various configurations such as Reddy et al. [10] who investigated the importance of the Soret and Hall effects on Casson fluid toward a vertical surface. The dimensional equations that control flow were converted into dimensionless equations by dimensionless variables, leading to the discovery of the analytical solution via the homotopy analysis method (HAM), which was then contrasted with the Adomain decomposition method (ADM) solution. With a particular focus on the physical factors involved in the current investigation, the heat and mass transfer rates against the Casson fluid parameter were visually illustrated. When the upper disk is assumed to be impermeable and the bottom one is assumed to be porous, Mohyud-Din and Khan [11] explored the time-dependent Casson fluid flow. The controlling equations were transformed by using transformations. The formulas for the temperature and velocity were obtained using HAM. The effects of several physical parameters were explored towards Eckert, squeeze numbers, and dimensionless length. The system's overall inaccuracy was calculated for both the suction and injection situations using Mathematica Package BVPh2.0. For emerging parameters, surface quantities were reported. For both the presence and absence of a magnetic field, Casson fluid was studied by Abro and Khan [12]. The Fabrizio–Caputo fractional derivative was used to obtain the flow formulation. Analytical solutions were identified. The Fox-H

and Mittag–Leffler functions were used to express the generic solutions for the flow field. Finally, a graphical representation was provided using the relevant parameters, and it was seen that the behavior of the Caputo–Fabrizio and ordinary fractional fluid models for the fluid flow was reciprocal. The analysis of time independent naturally convective flow was identified by Kataria and Patel [13]. A vertical plate was passed over by a Casson fluid flow. The flow equations were resolved numerically in Matlab and resolved analytically using the Laplace transform method. Sherwood, Nusselt numbers, and skin friction expressions were discovered. By creating graphs, the properties of the flow field were examined, and the physical elements were thoroughly explained. The examination of the Casson liquid over a disk as a semi-infinite zone was presented by Rehman et al. [14]. The Casson nano-liquid flow was achieved by rotating a rigid disk at a fixed angular frequency. By creating a homogenous magnetic field normal to the axial direction, magnetic interaction was taken into consideration. The chemical reaction, heat generation, heat absorption, and Navier's slip condition were manifested during disk rotation. In order to create an ordinary differential system, the obtained flow narrating differential equations was reduced. The Von Karman method of the scheme was used to achieve this. Instead of continuing with the standard built-in system, a computational approach was developed to produce correct trends. By using graphical and tabular structures, the effects of the flow parameters were studied. It was found that the Casson fluid parameter caused both the tangential and radial velocities to decrease. Neeraja et al. [15] explored convective and viscous dissipation effects on magnetized Casson fluid. Using the gunshot method, the flow equations were resolved. The governing parameters affected the temperature, solid displacement, liquid velocity, and concentration. For the Casson parameter, the liquid velocity and consequently the solid displacement were reduced. When compared to the previous results, the current results showed a logical agreement. In the context of emerging mass and heat transfer technologies, Rasool et al. [16] examined the properties of Casson nanofluid flow via porous media across a non-linear stretching surface. The Darcy–Forchheimer relation allows for an incompressible viscous nanofluid of the Casson type to pass through the specified porous material. For the nanoparticles' velocity, temperature, and concentration, slip boundary conditions were applied. Attendance was made to Brownian diffusion and thermophoresis. To numerically solve the problem, a Runge–Kutta (RK) scheme of fourth order was used. Graphs were created for a range of progressive non-dimensionalized parameter values, and numerical data were used to examine changes in wall drag factor, heat transfer rates, and mass transfer rates. The results show that the porous media offer resistance to fluid flow and the strength of the inertial impact decreases the momentum boundary layer. The thermophoresis and Brownian motion were discovered to have a progressive relationship with temperature. For increasing values of the slip parameters, there is a decrease in the magnitude of the rate of heat and mass transfers. Over a horizontal plate the Casson nanofluid flow through use of the non-Darcy porous medium, Farooq et al. [17] reported their findings. By utilizing the proper non-similar transformations, the equations were converted into a dimensionless model. Through the use of bvp4c, local non-similarity was used to solve the dimensionless partial differential system. In-depth research was carried out on the effects of the newly discovered non-dimensional characteristics on the flow field. Additionally, the influences of variables on the skin friction and the rate of heat transfer were investigated. Finally, using publicly available data, comparisons between locally similar solutions and non-similar solutions were completed. Ramesh et al. [18] investigated the time-dependent and incompressible Casson squeezing flow in between disks. In the flow phenomena, the nanofluid theory (Buongiorno model) was realized. For the lower disks, concentration, temperature, and velocity slip were also included. The similarity functions were completed first to ultimate flow equations and they were solved by the RK-5 scheme. The results were presented in relation to the various physical quantities. A higher Reynolds number caused a decline in radial velocity. The vortex viscosity parameter first increases and subsequently decreases the microrotational field.

Owing to the importance of the Casson fluid model, artificial neural networking models are constructed for two different boundary layer flow regimes, namely non-magnetized and magnetized flow fields. The Casson fluid flow towards the stretching cylinder is mathematically formulated in the presence of a heat generation effect, viscous dissipation, mixed convection, temperature-dependent variable thermal conductivity, thermal radiations, and first-order chemical reaction effects. The ultimate flow equations are solved by the use of the shooting method. The skin friction coefficient (SFC) is estimated at the cylindrical surface. We constructed artificial neural networking models for better estimation of the skin friction coefficient. We believe that by following the present outcomes of the Casson fluid flow regime, one can extend the idea to investigate the time-independent shear rate and shear stress characteristics of molten chocolate, yogurt, blood, and many other culinary and biological materials. The present research contributes to answering the following concerns:

- Formulation of Casson fluid flow towards cylindrical surfaces with pertinent physical effects.
- Comparative examination of Casson velocity for magnetized and non-magnetized flow fields.
- Examination of Casson concentration for chemically reactive and non-reactive flow fields.
- Evaluation of the SFC at the cylindrical surface for non-magnetized and magnetized flow fields.
- Estimation of the SFC by using an artificial neural networking model.

2. Mathematical Formulation

The Casson fluid flow field is considered towards the inclined surface in the presence of mixed convection, a magnetic field, and stagnation point flow. Both heat and mass transfer aspects are considered for better novelty. Thermal effects, namely thermal radiations, viscous dissipation, variable thermal conductivity, and heat generation, are considered by way of an energy equation while the first-order chemical reaction effect is calculated by the use of a concentration equation. Both the concentration and temperature at the cylindrical surface are presumed higher in strength as compared to the field far away from the surface.

The geometry of the problem is given in Figure 1a. The ultimate mathematical equations [19,20] for the present problem are stated as follows:

$$\frac{\partial(\widetilde{R}\widetilde{U})}{\partial\widetilde{X}} + \frac{\partial(\widetilde{R}\widetilde{V})}{\partial\widetilde{R}} = 0\,, \tag{1}$$

$$\begin{aligned}\widetilde{U}\frac{\partial\widetilde{U}}{\partial\widetilde{X}} + \widetilde{V}\frac{\partial\widetilde{U}}{\partial\widetilde{R}} &= \nu\left(1+\tfrac{1}{\beta}\right)\left(\frac{\partial^2\widetilde{U}}{\partial\widetilde{R}^2} + \frac{1}{\widetilde{R}}\frac{\partial\widetilde{U}}{\partial\widetilde{R}}\right) + g_0\beta_T(\widetilde{T}-\widetilde{T}_\infty)cos(\alpha)\\ &+g_0\beta_C(\widetilde{C}-\widetilde{C}_\infty)cos(\alpha) + \widetilde{U}_e\frac{\partial\widetilde{U}_e}{\partial\widetilde{X}} - \frac{\sigma B_0^2}{\rho}(\widetilde{U}-\widetilde{U}_e)\,,\end{aligned} \tag{2}$$

$$\rho c_\rho\left(\widetilde{U}\frac{\partial\widetilde{T}}{\partial\widetilde{X}} + \widetilde{V}\frac{\partial\widetilde{T}}{\partial\widetilde{R}}\right) = \frac{1}{\widetilde{R}}\frac{\partial}{\partial\widetilde{R}}\left(\kappa\frac{\partial\widetilde{T}}{\partial\widetilde{R}}\right) - \frac{1}{\widetilde{R}}\frac{\partial}{\partial\widetilde{R}}\left(\widetilde{R}\overline{q}\right) + \overline{\mu}\left(1+\frac{1}{\beta}\right)\left(\frac{\partial\widetilde{U}}{\partial\widetilde{R}}\right)^2 + Q_0\left(\widetilde{T}-\widetilde{T}_\infty\right). \tag{3}$$

$$\widetilde{U}\frac{\partial\widetilde{C}}{\partial\widetilde{X}} + \widetilde{V}\frac{\partial\widetilde{C}}{\partial\widetilde{R}} = D_m\frac{\partial^2\widetilde{C}}{\partial\widetilde{R}^2} - k_c(\widetilde{C}-\widetilde{C}_\infty). \tag{4}$$

In Equations (1)–(4), B_0 is the uniform magnetic field, D_m is the mass diffusivity, $\widetilde{C}$ is the concentration, β_C denotes the solutal expansion coefficient, β_T is the thermal expansion coefficient, and k_c is the rate of the chemical reaction,. The relation for radioactive heat flux is given as:

$$\overline{q} = -\frac{\partial\widetilde{T}}{\partial\widetilde{R}}\ \frac{16\sigma^*T_\infty^3}{3k^*}\,. \tag{5}$$

The variable thermal conductivity relation is given as:

$$\kappa\left(\widetilde{T}\right) = \left(\varepsilon\frac{\widetilde{T}-\widetilde{T}_\infty}{\Delta T}+1\right)\kappa_\infty, \tag{6}$$

with

$$\Delta T = \widetilde{T}_w - \widetilde{T}_\infty. \tag{7}$$

The flow endpoint conditions are particularized as:

$$\widetilde{U}(\widetilde{X},\widetilde{R}) = \widetilde{U}_w = a\widetilde{X},\ \widetilde{V}(\widetilde{X},\widetilde{R}) = 0\ ,\widetilde{C} = \widetilde{C}_w,\ \widetilde{T} = \widetilde{T}_w,\ \text{at}\ \widetilde{R} = R_1\ , \tag{8}$$

$$\widetilde{U} = \widetilde{U}_e = d\widetilde{X}\ ,\ \widetilde{C}\to\widetilde{C}_\infty,\ \widetilde{T}\ \to\widetilde{T}_\infty,\quad \text{as}\ \ \widetilde{R}\to\infty\ . \tag{9}$$

To obtain a reduced differential system, we have:

$$\begin{gathered}\widetilde{U} = \widetilde{X}\frac{U_0}{L}F'_C(\eta),\ \widetilde{V} = -\frac{R_1}{\widetilde{R}}\sqrt{\frac{\nu U_0}{L}}F_C(\eta),\\ \theta_C(\eta) = \frac{\widetilde{T}-\widetilde{T}_\infty}{\widetilde{T}_w-\widetilde{T}_\infty},\ \phi_C(\eta) = \frac{\widetilde{C}-\widetilde{C}_\infty}{\widetilde{C}_w-\widetilde{C}_\infty},\ \eta = \frac{\widetilde{r}^2-{R_1}^2}{2R_1}\sqrt{\frac{U_0}{\nu L}}\ .\end{gathered} \tag{10}$$

With Equation (10) in Equations (2)–(4), we obtain:

$$\begin{gathered}(1+1/\beta)(F_C'''(1+2\gamma\eta)+2\gamma F_C'') - {F_C'}^2 + F_C F_C'' + G_T\theta_C\cos(\alpha) + G_C\phi_C\cos(\alpha)\\ -M^2(F_C'-A)+A^2 = 0\ ,\end{gathered} \tag{11}$$

$$\begin{gathered}\left(1+\tfrac{4}{3}R\right)\left(\theta_C''(1+2\eta\gamma)+2\gamma\theta_C'\right)+\varepsilon\left((\theta_C\theta_C''+{\theta_C'}^2)(1+2\eta\gamma)+2\gamma\theta_C\theta_C'\right)\\ +\mathrm{Pr}E(1+2\eta\gamma)\left(1+\tfrac{1}{\beta}\right){F_C''}^2+\mathrm{Pr}H\theta_C+\mathrm{Pr}F_C\theta_C' = 0\ ,\end{gathered} \tag{12}$$

$$\phi_C''(1+2\eta\gamma)+2\gamma\phi_C'+Scf\phi_C'-ScRc\phi_C = 0\ , \tag{13}$$

The reduced endpoint conditions are:

$$F_C = 0,\ {F_C}' = 1\ ,\theta_C = 1,\phi_C = 1,\text{at}\ \eta = 0 \tag{14}$$

$${F_C}' = A,\ \theta_C = 0,\ \phi_C = 0,\ \text{as}\ \eta\to\infty\ . \tag{15}$$

The flow parameters are identified as:

$$\begin{gathered}\beta = \frac{\overline{\mu}\sqrt{2\pi_c}}{\tau_r},\ R = \frac{4\sigma^*\widetilde{T}_\infty^3}{\kappa k^*},\ A = \frac{d}{a},\gamma = \sqrt{\frac{\upsilon L}{c^2U_0}},\\ G_C = \frac{g_0\beta_C(\widetilde{C}_w-\widetilde{C}_\infty)L^2}{U_0\widetilde{x}},\ G_T = \frac{g_0\beta_T(\widetilde{T}_w-\widetilde{T}_\infty)L^2}{U_0\widetilde{x}},\ M = \sqrt{\frac{\sigma B_0^2L}{\rho U_0}},\ Pr = \frac{\overline{\mu}c_p}{\kappa},\\ E = \frac{U_0^2(\widetilde{x}/L)^2}{c_p(\widetilde{T}_w-\widetilde{T}_\infty)},\ H = \frac{LQ_0}{U_0\rho c_p}\ ,\ Sc = \frac{\nu}{D_m},\ \ Rc = \frac{k_cL}{U_0}.\end{gathered} \tag{16}$$

The chemical reaction parameter, radiation, magnetic field, heat generation parameters, Prandtl, Schmidt, Eckert, concentration Grashof, temperature Grashof numbers, Casson fluid parameter, curvature parameter, and velocities ratio parameter are symbolized as Rc, R, M, H, Pr, Sc, E, G_C, G_T, β, γ and A, respectively. For the present case, our interest lies in evaluating the SFC at the cylindrical surface. Therefore, the mathematical relationship for SFC is as followes:

$$\left.\begin{array}{l}C_f = \frac{2\tau_w}{\rho U_w^2}\ ,\\ \tau_w = \overline{\mu}\left(\frac{\partial\widetilde{u}}{\partial\widetilde{r}}\right)_{\widetilde{r}=c},\\ \sqrt{\mathrm{Re}_{\widetilde{x}}}C_f = \left(1+\frac{1}{\beta}\right)f''\ (0)\end{array}\right\}. \tag{17}$$

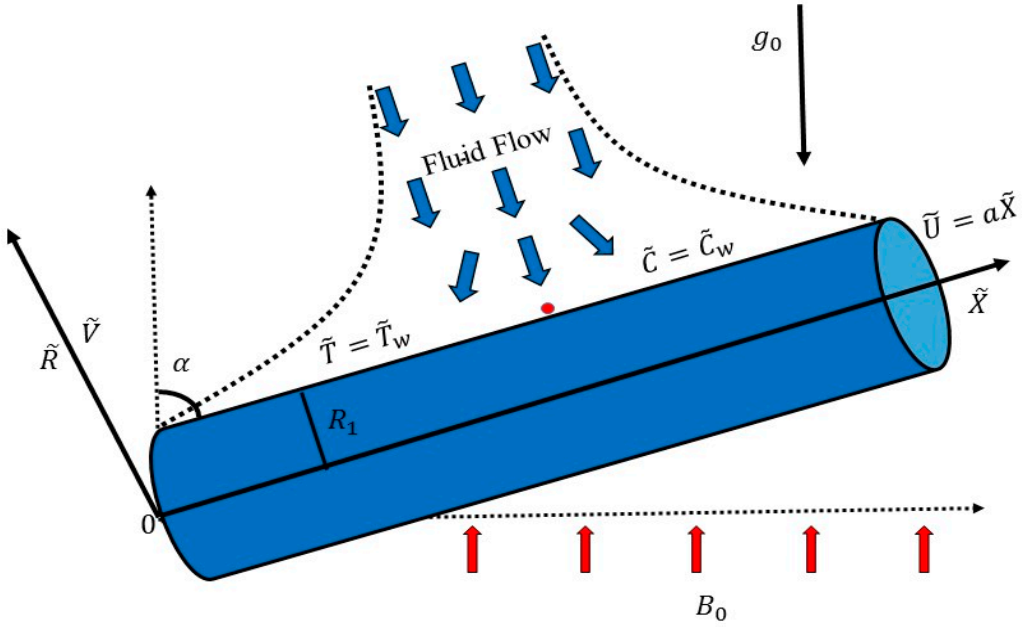

(**a**)

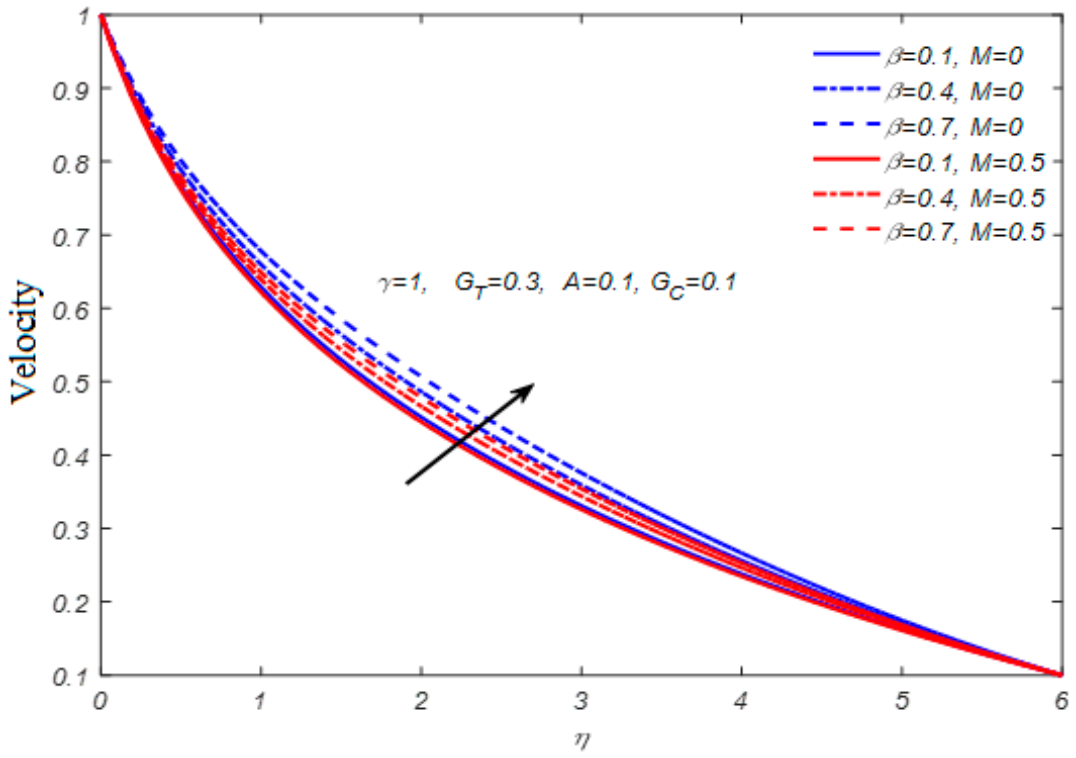

(**b**)

Figure 1. *Cont.*

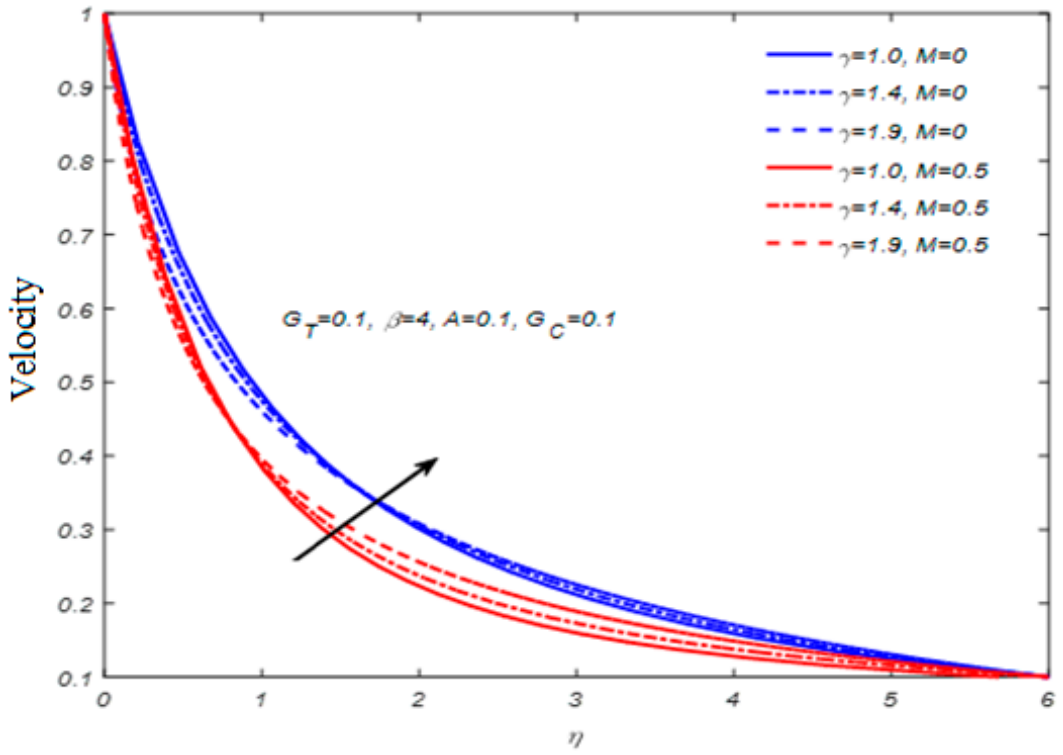

(**c**)

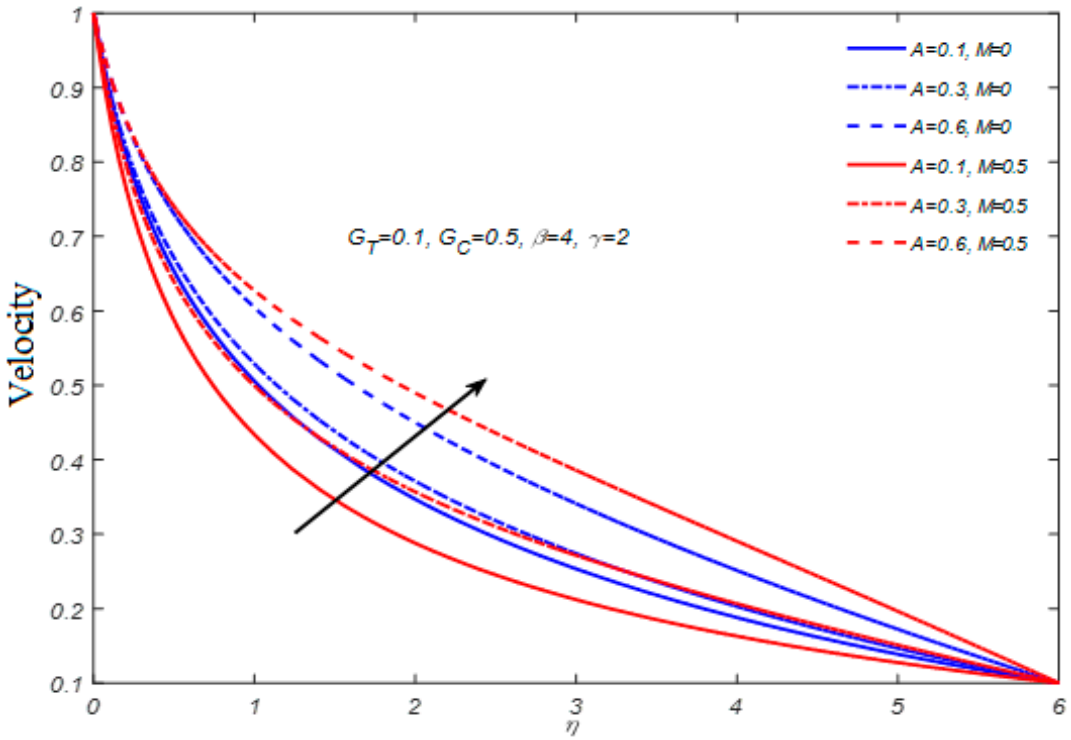

(**d**)

Figure 1. (**a**) Geometry of the problem. (**b**) Impact of β on $f'(\eta)$. (**c**) Impact of γ on $f'(\eta)$. (**d**) Impact of A on $f'(\eta)$.

3. Non-Magnetized Mathematical Model

The heat transfer characteristics in the magnetized flow field of Casson fluid at the cylindrical surface are considered. Mixed convection, stagnation point flow, viscous dissipation, heat generation, variable thermal conductivity, thermal radiation effects, and first-order chemical reaction effects are combined for better novelty. The flow narrating the differential system for a non-magnetized flow regime can be obtained by using $M = 0$ in Equations (11)–(15) and we have:

$$(1+1/\beta)(F_C'''(1+2\gamma\eta)+2\gamma F_C'')+F_C F_C''-{F_C'}^2+G_T\theta_C\cos(\alpha)+G_C\phi_C\cos(\alpha)+A^2=0\,, \tag{18}$$

$$\left(1+\tfrac{4}{3}R\right)\left(\theta_C''(1+2\eta\gamma)+2\gamma\theta_C'\right)+\varepsilon\Big((\theta_C\theta_C''+{\theta_C'}^2)(1+2\eta\gamma)+2\gamma\theta_C\theta_C'\Big) \tag{19}$$

$$+\mathrm{Pr}E(1+2\eta\gamma)\left(1+\tfrac{1}{\beta}\right){F_C''}^2+\mathrm{Pr}H\theta_C+\mathrm{Pr}F_C\theta_C'=0\,,$$

$$\phi_C''(1+2\eta\gamma)+2\gamma\phi_C'+Scf\phi_C'-ScRc\phi_C=0\,, \tag{20}$$

The boundary conditions for the present cases remain the same:

$$F_C=0,\ F_C'=1\ ,\theta_C=1,\phi_C=1,\text{ at }\eta=0 \tag{21}$$

$$F_C'=A,\ \theta_C=0,\ \phi_C=0,\text{ as }\eta\to\infty\,. \tag{22}$$

It is important to note that for the evaluation of SFC, see Equation (17) to see that the mathematical relationship remains the same.

4. Solution Methodology

The flow equations are highly non-linear therefore one cannot obtain an exact solution. For the numerical solution, we choose the shooting scheme along with the Runge–Kutta algorithm due to higher convergence. To implement the shooting method [21,22], we need to transform Equations (11)–(15) into a set of first-order initial value systems (IVSs). To achieve such IVSs, we considered:

$$\begin{aligned} &Y_1=F_C(\eta),\ Y_2=F_C'(\eta),\quad Y_3=F_C''(\eta),\quad Y_4=\theta_C(\eta),\\ &Y_5=\theta_C'(\eta),Y_6=\phi_C(\eta),\quad Y_7=\phi_C'(\eta), \end{aligned} \tag{23}$$

Using Equation (23) into Equations (11)–(15), we have:

$$Y_1'=Y_2, \tag{24}$$

$$Y_2'=Y_3, \tag{25}$$

$$Y'_3=\frac{1}{\left(1+\frac{1}{\beta}\right)(1+2\eta\gamma)}\left[\begin{array}{l}-2\gamma Y_3\left(1+\frac{1}{\beta}\right)+Y_2^2-Y_1Y_3-G_TY_4\cos\alpha-G_CY_6\cos\alpha\\ -M^2(Y_2-A)-A^2\end{array}\right], \tag{26}$$

$$Y_4'=Y_5, \tag{27}$$

$$Y_5'=-\frac{1}{\left(1+\frac{4}{3}R\right)(1+2\eta\gamma)+\varepsilon(1+2\eta\gamma)Y_4}\left[\begin{array}{l}(1+\frac{4}{3}R)(2\gamma Y_5)+\varepsilon((1+2\eta\gamma)Y_5^2+2\gamma Y_4Y_5)+\\ \mathrm{Pr}Y_1Y_5+\mathrm{Pr}E(1+2\eta\gamma)(1+\frac{1}{\beta})Y_3^2+\mathrm{Pr}HY_4\end{array}\right], \tag{28}$$

$$Y_6'=Y_7, \tag{29}$$

$$Y_7'=\frac{ScRcY_6-ScY_1Y_6-2\gamma Y_7}{(1+2\eta\gamma)}. \tag{30}$$

Meanwhile, the conditions are transformed as:

$$\begin{aligned} Y_6 = 1, Y_4 = 1, Y_2 = 1,\ Y_1 = 0, \quad \text{at} \quad \eta = 0, \\ Y_6 \to 0, Y_4 \to 0\ ,\ Y_2 \to A, \quad \text{as} \quad \eta = \infty. \end{aligned} \tag{31}$$

5. Numerical Outcomes

The numerical outcomes are detailed as line graphs and tables. Figure 1b–d is plotted for the examination of velocity while Figure 2a,b offers the concentration outcomes. In detail, for the velocity analysis, two separate flow fields, namely the magnetic flow field and the non-magnetic flow field, are taken into consideration. We possess a non-magnetic flow field by selecting $M = 0$ and $M = 0.5$ for the magnetic regime. For velocity dependency, we focused on the following inputs, namely the curvature, Casson fluid [23], and velocities ratio parameters for these two regimes.

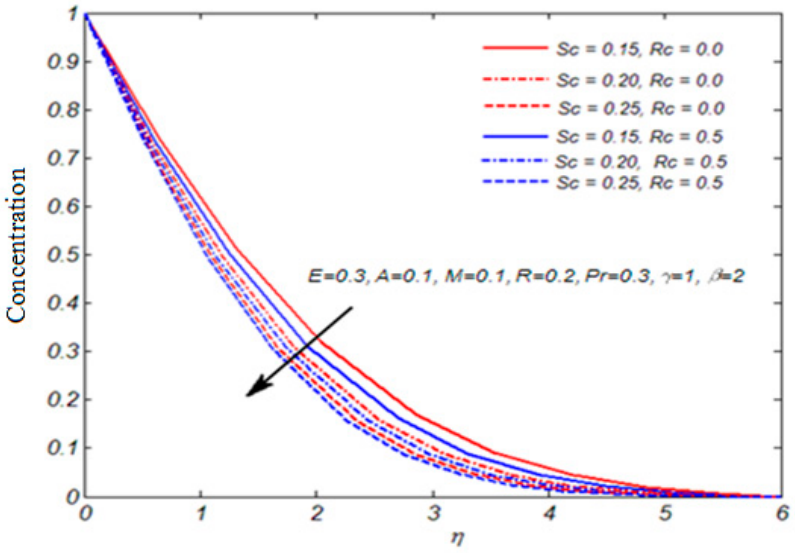

(**a**)

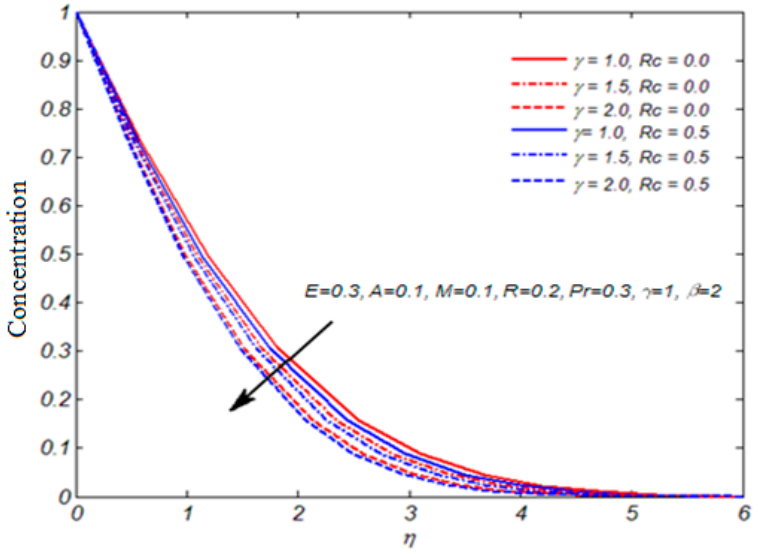

(**b**)

Figure 2. (**a**) Impact of Sc on $\phi(\eta)$. (**b**) Impact of γ on $\phi(\eta)$.

Figure 1b displays the influence of the Casson fluid parameter on the velocity in scenarios involving magnetic and non-magnetic fields. For higher Casson parameters, the velocity profile significantly increases. Both magnetic and non-magnetic fluid flows have the same effect. It is important to remember that greater Casson fluid parameter values cause the viscosity to decrease and as a result the velocity increases. In addition, it should be noted that the velocity is greater for a non-magnetic flow regime than it is in a magnetic flow field. When an external magnetic field was taken into consideration, the Lorentz force existed as a resistive force. The effect of the curvature parameter on the Casson fluid velocity is shown in Figure 1c for the flow regimes. The Casson fluid velocity noticeably increases for positive variations in the curvature parameter, and this effect is shared by both flow fields. This is due to the fact that the radius of the curvature decreases when the curvature parameter is iterated positively. As a result, there is less of a surface area in contact with the fluid flow, resulting in reduced resistance for the fluid particles. It is important to keep in mind that the strength of the velocity is higher for non-magnetic flow fields than for magnetic flow fields. This is because of Lorentz force's existence when a magnetic field is applied externally.

The effect of the velocities ratio is seen in Figure 1d. We have seen that the Casson fluid velocity is directly dependent on the velocities ratio parameter, and that larger values in the velocities ratio parameter led to higher magnitudes of fluid velocity. It is key to remember that the velocities ratio parameter is the ratio of free stream velocity to stretching velocity. When the ratio parameter has a value lower than one, it is inferred that the role of the free stream is less important than the stretching velocity. As a result, the inclined stretched cylindrical surface causes a considerable disturbance in fluid flow. It is necessary to keep in mind that the effect of the velocities ratio parameter on the Casson fluid flow is the same for the magnetic and non-magnetic flow fields for the stagnation point flow. The study of the impact of flow parameters on Casson fluid concentration is seen in Figure 2a,b. For the purpose of examining concentrations, we specifically took into account the reactive and non-reactive flows. We take $Rc = 0$ for a non-reactive flow field and $Rc = 0.5$ for a chemically reactive environment.

We took into account differences in the curvature parameter and Schmidt number for these two regimes. The combined effect of the Sc on the concentration for reactive and non-reactive scenarios is depicted in Figure 2a. We noticed that the concentration profile greatly declines for higher values of the Schmidt number. Both reactive and non-reactive fluid flow scenarios have the same effect. In addition, it is important to remember that the strength of the concentration profile is higher in the case of a reactive flow regime than it is in a non-reactive flow field. The influence of the curvature parameter on the concentration of Casson fluid is shown in Figure 2b for both reactive and non-reactive flow patterns.

The Casson fluid concentration decreases noticeably for positive variations In the curvature parameter, as we have seen. The effects are the same in both flow fields. This is because the radius of curvature decreases when we iterate the curvature parameter affirmatively. As a result, there is a reduced surface area in contact with the fluid flow, which lowers the resistance that the fluid particles must overcome. In the current flow problem, SFC is physical quantity at cylindrical surfaces; see Tables 1–8. The deviation in skin friction is noticed when chemically reactive Casson fluid flow at cylindrical surfaces is assumed along with magnetic, mixed convection, stagnation point flow, heat generation, viscous dissipation, and variable thermal conductivity effects. Tables 1–8 offer an investigation into the impact of flow parameters on skin friction for two distinct values of the magnetic field parameter, $M = 0$, and $M = 0.2$. In detail, Tables 1 and 2 provide an analysis of the effect of the Casson fluid parameter [24] on the SFC.

Here, $M = 0$ denotes the flow of non-magnetized Casson fluid, whereas $M = 0.2$ denotes the flow of magnetized Casson fluid. Tables 1 and 2 demonstrate that the SFC exhibits a decreasing trend as the Casson fluid parameter values increase. These findings hold true for both flow fields. It is noticeable that the magnetic flow field has stronger skin friction coefficients than the non-magnetic flow field. The fluctuation in the SFC for positive

variations in the velocities ratio parameter is shown in Tables 3 and 4. Such observations are evaluated for both flow fields. We have seen that the SFC decreases noticeably for higher values of the velocities ratio parameter. Additionally, in the case of non-magnetized Casson fluid, the SFC is lower in magnitude. For two distinct values of the magnetic field parameter, Tables 5 and 6 display the impact of the curvature parameter on the SFC. We have seen that the SFC considerably rises with an increasing curvature parameter.

It should be noted that for magnetic flow fields, the skin friction coefficient values are higher. The fluctuation in the SFC for positive values of the thermal Grashof number is seen in Tables 7 and 8. We have seen that as for initial values of the thermal Grashof number, the skin friction coefficient tends to decrease but for positive values of the thermal Grashof number, the SFC increases. It can be seen that the strength of skin friction is substantially higher for non-magnetic flow fields than for magnetic flows.

Table 1. Impact of the Casson fluid parameter on the SFC for the nonmagnetic flow field.

β	$f''(0)$	$(1+1/\beta)f''(0)$	**ANN Values**
	$M = 0$	$M = 0$	$M = 0$
0.2	−0.8224	−4.9344	5.205703
0.3	−0.8633	−3.7409	3.64113
0.4	−0.8965	−3.1377	3.207106
0.5	−0.9241	−2.7723	2.685965
0.6	−0.9474	−2.5264	2.468694
0.7	−0.9673	−2.3492	2.21511
0.8	−0.9846	−2.2154	2.107406
0.9	−0.9998	−2.1106	2.041828
1.0	−1.0131	−2.0262	1.926957
2.0	−1.0928	−1.6392	1.526076

Table 2. Impact of the Casson fluid parameter on the SFC for the magnetic flow field.

β	$f''(0)$	$(1+1/\beta)f''(0)$	**ANN Values**
	$M = 0.2$	$M = 0.2$	$M = 0.2$
0.2	−0.8517	−5.1102	5.127272
0.3	−0.9017	−3.9074	3.906281
0.4	−0.9420	−3.1377	3.142552
0.5	−0.9752	−2.9256	2.913623
0.6	−1.0039	−2.6771	2.689821
0.7	−1.0271	−2.4944	2.491419
0.8	−1.0478	−2.3575	2.352806
0.9	−1.0659	−2.2503	2.252857
1.0	−1.0818	−2.1639	2.16358
2.0	−1.1763	−2.3526	2.370091

Table 3. Impact of the velocities ratio parameter on the SFC for the nonmagnetic flow field.

A	$f''(0)$	$(1+1/\beta)f''(0)$	ANN Values
	$M = 0$	$M = 0$	$M = 0$
0.2	−0.4365	−1.8913	1.798471
0.3	−0.4153	−1.7995	1.775878
0.4	−0.3859	−1.6721	1.761253
0.5	−0.3486	−1.5105	1.47786
0.6	−0.3036	−1.3154	1.397436
0.7	−0.2511	−1.0881	1.114926
0.8	−0.1914	−0.8293	0.84088
0.9	−0.1245	−0.5395	0.560701
1.0	−0.0497	−0.2154	0.221825
2.0	−0.0097	−0.0421	0.044358

Table 4. Impact of the velocities ratio parameter on the SFC for the nonmagnetic flow field.

A	$f''(0)$	$(1+1/\beta)f''(0)$	ANN Values
	$M = 0.2$	$M = 0.2$	$M = 0.2$
0.2	−0.4757	−2.0612	2.061184
0.3	−0.4457	−1.9312	1.937046
0.4	−0.4081	−1.7683	1.776405
0.5	−0.3633	−1.5742	1.580536
0.6	−0.3114	−1.3494	1.351205
0.7	−0.2526	−1.0945	1.090686
0.8	−0.1871	−0.8107	0.81182
0.9	−0.1146	−0.4965	0.498124
1.0	−0.0344	−0.1491	0.150031
2.0	−0.0067	−0.0291	0.028967

Table 5. Impact of the curvature parameter on the SFC for the nonmagnetic flow field.

γ	$f''(0)$	$(1+1/\beta)f''(0)$	ANN Values
	$M = 0$	$M = 0$	$M = 0$
0.2	−0.5089	−2.2052	2.054256
0.3	−0.5595	−2.4243	2.433774
0.4	−0.6068	−2.6293	2.688039
0.5	−0.6523	−2.8264	2.789083
0.6	−0.6965	−3.0179	3.168692
0.7	−0.7396	−3.2046	3.04553
0.8	−0.7820	−3.3884	3.265665
0.9	−0.8236	−3.5686	3.535665
1.0	−0.8647	−3.7467	3.75129
2.0	−1.2520	−5.4249	5.194255

Table 6. Impact of the curvature parameter on the SFC for the magnetic flow field.

γ	$f''(0)$	$(1+1/\beta)f''(0)$	ANN Values
	$M = 0.2$	$M = 0.2$	$M = 0.2$
0.2	−0.5547	−2.4035	2.397728
0.3	−0.6038	−2.6163	2.618119
0.4	−0.6499	−2.8161	2.820131
0.5	−0.6944	−3.0088	3.010963
0.6	−0.7377	−3.1964	3.195347
0.7	−0.7800	−3.3797	3.376525
0.8	−0.8216	−3.5599	3.55692
0.9	−0.8626	−3.7376	3.738581
1.0	−0.9030	−3.9126	3.923491
2.0	−1.2857	−5.5709	5.600951

Table 7. Impact of the temperature Grashof number on the SFC for the nonmagnetic flow field.

G_T	$f''(0)$	$(1+1/\beta)f''(0)$	ANN Values
	$M = 0$	$M = 0$	$M = 0$
0.2	−0.3822	−1.6561	1.545852
0.3	−0.3107	−1.3463	1.296924
0.4	−0.2319	−1.0048	1.027428
0.5	−0.1363	−1.0016	0.938263
0.6	−1.1515	−4.9894	5.305239
0.7	−1.1315	−4.9027	4.950683
0.8	−1.1115	−4.8162	4.683114
0.9	−1.0715	−4.6428	4.742156
1.0	−1.0915	−4.7295	4.449012
2.0	−2.0515	−8.8892	8.987435

Table 8. Impact of the temperature Grashof number on the SFC for the magnetic flow field.

G_T	$f''(0)$	$(1+1/\beta)f''(0)$	ANN Values
	$M = 0.2$	$M = 0.2$	$M = 0.2$
0.2	−0.8802	−3.8139	3.786153
0.3	−0.8563	−3.7103	3.708539
0.4	−0.8324	−3.6067	3.609377
0.5	−0.8084	−3.5027	3.498244
0.6	−0.7845	−3.3993	3.403159
0.7	−0.7606	−3.2956	3.298737
0.8	−0.7367	−3.1921	3.187463
0.9	−0.7128	−3.0885	3.082916
1.0	−0.6889	−2.9850	2.986601
2.0	−0.4509	−1.9537	1.955074

6. Artificial Neural Networking Outcomes

The Casson flow field was mathematically modelled and solved by use of the shooting method. At the surface, skin friction is a quantity of interest. We evaluated the values of the skin friction coefficient at the cylindrical surface by assuming two different flow regimes.

In the first case, we considered the flow regime without an externally applied magnetic field while in another case the flow regime was assumed in the presence of the externally applied magnetic field. For both cases, we have developed an artificial neural networking (ANN) model. For a non-magnetic flow field, we selected $M = 0$, and for the magnetic flow field, we selected $M = 0.2$. Multilayer perceptron (MLP) is used because of its strong structural characteristics. MLP networks are made up of layers, and each layer is coupled to the next. Because the input factors influencing each estimated skin friction coefficient

(SFC) value vary, two distinct ANN models were created, with distinct input and output values produced for each. Figure 3a depicts the MLP architecture, which depicts the layered structure of the produced ANN models. Table 9 shows the input and output parameters for each generated model. It is critical to optimize the data set used in the construction of ANN models [25]. Seventy percent of the data set used to create the two separate models was set aside for training, 15% for validation, and 15% for testing [26]. One of the challenges in developing ANN models is the lack of a rule for identifying the neurons in the hidden layer [27]. Figure 3b,c depicts the structural topologies of two different ANN models. From both figures, one can see that four input values are defined in the input layer of each of the given structural topologies, while the number of neurons in the hidden layers is 20 and 10, respectively. In the output layer, it is seen that the SFC parameter, which is the only value, is obtained. For ANN models, it is important to ideally optimize the data set being used [28]. Seventy percent of the data set used for the two different models developed was reserved for training the model, 15% for testing, and 15% for validation. The lack of a set formula for calculating the number of neurons in the hidden layer is one of the challenges in designing ANN models. For this reason, the performance of ANN models with different numbers of neurons in the hidden layer has been examined and the number of neurons in the hidden layer has been ideally optimized.

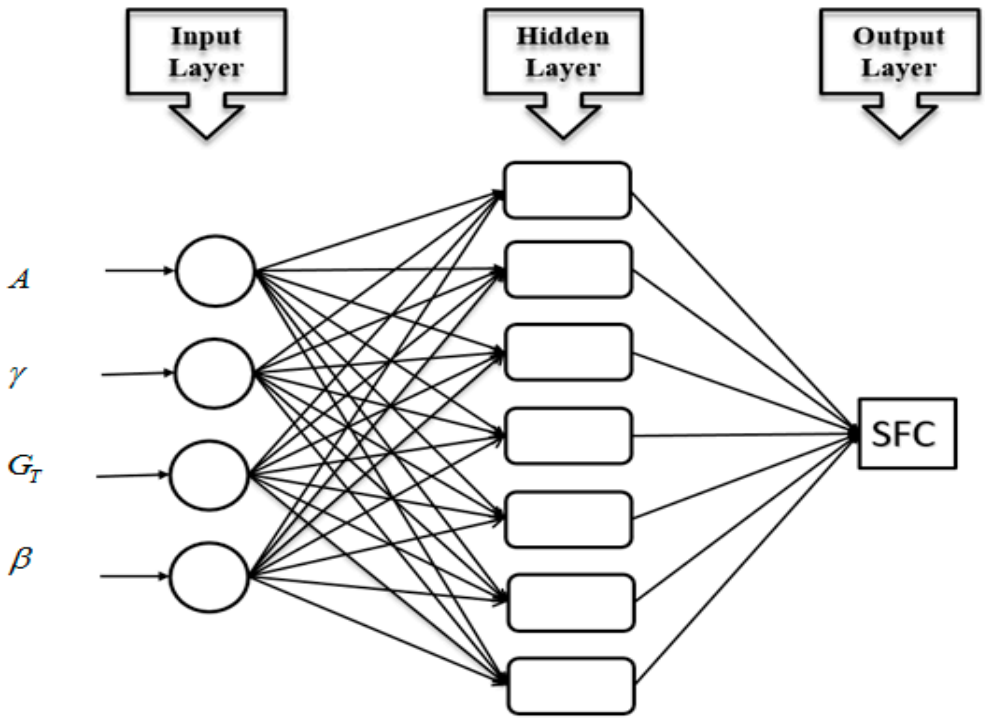

(**a**)

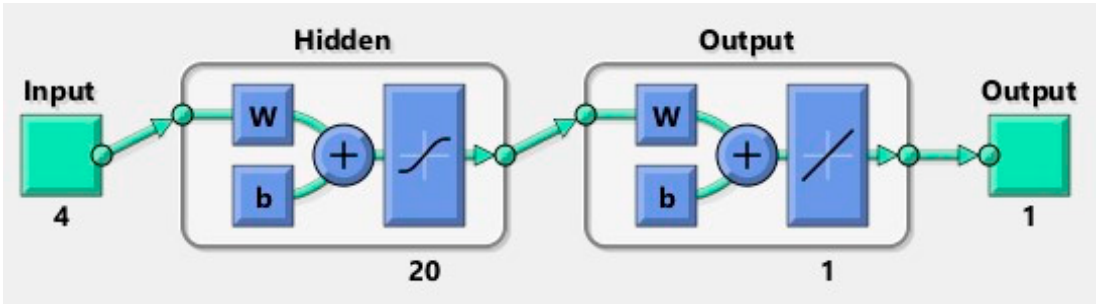

(**b**)

Figure 3. *Cont.*

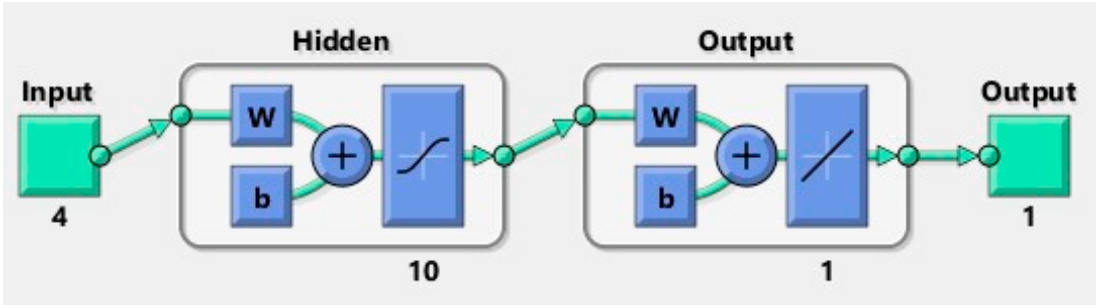

(**c**)

Figure 3. (**a**) The layered structure of the developed ANN models for SFC. (**b**) Structural topology of the ANN model for the non-magnetized flow field. (**c**) Structural topology of the ANN model for the magnetized flow field.

Table 9. The output and input parameters for each developed model.

Model	Inputs				Output
Model 1 ($M = 0$)	A	γ	G_T	β	SFC
Model 2 ($M = 0.2$)	A	γ	G_T	β	SFC

Table 10 contains information about the data set utilized in each ANN model as well as the number of neurons in each models hidden layer. The Levenberg–Marquardt training technique, which is extensively utilized due to its great learning performance, is used in MLP network models. The hidden and output layers both have access to purelin and tan–sig transfer functions. The following are the mathematical expressions for the transfer functions utilized:

$$f(x) = \frac{1}{1 + \exp(-x)}, \tag{32}$$

$$\text{purelin}(x) = x. \tag{33}$$

Table 10. Information about the data set used in each ANN model and the number of neurons.

Model	Number of Neuron	Training	Validation	Test	Total
Model 1 ($M = 0$)	20	28	6	6	40
Model 2 ($M = 0.2$)	10	28	6	6	40

Mean squared error (MSE), coefficient of determination (R), and margin of deviation (MoD) parameters, which are extensively used in the literature, were chosen to evaluate the performance of two different ANN models [29,30]. The mathematical equations used to calculate the performance parameters are as follows:

$$\text{MSE} = \frac{1}{N}\sum_{i=1}^{N}\left(X_{\text{targ(i)}} - X_{\text{pred(i)}}\right)^2, \tag{34}$$

$$\text{R} = \sqrt{1 - \frac{\sum_{i=1}^{N}\left(X_{\text{targ(i)}} - X_{\text{pred(i)}}\right)^2}{\sum_{i=1}^{N}\left(X_{\text{targ(i)}}\right)^2,}}, \tag{35}$$

$$\text{MoD}(\%) = \left[\frac{X_{\text{targ}} - X_{\text{pred}}}{X_{\text{targ}}}\right] \times 100. \tag{36}$$

The training accuracy of the ANN models designed to predict SFC values in two different situations has been thoroughly studied. Training performance graphs for two ANN models are shown in Figure 4a,b for $M = 0$ and $M = 0.2$, respectively. The graphs in both figures depict the training cycle (epoch) that occurs in an MLP network. Furthermore, the MSE values of each ANN model are greater at the start of the training period and drop as the model progresses.

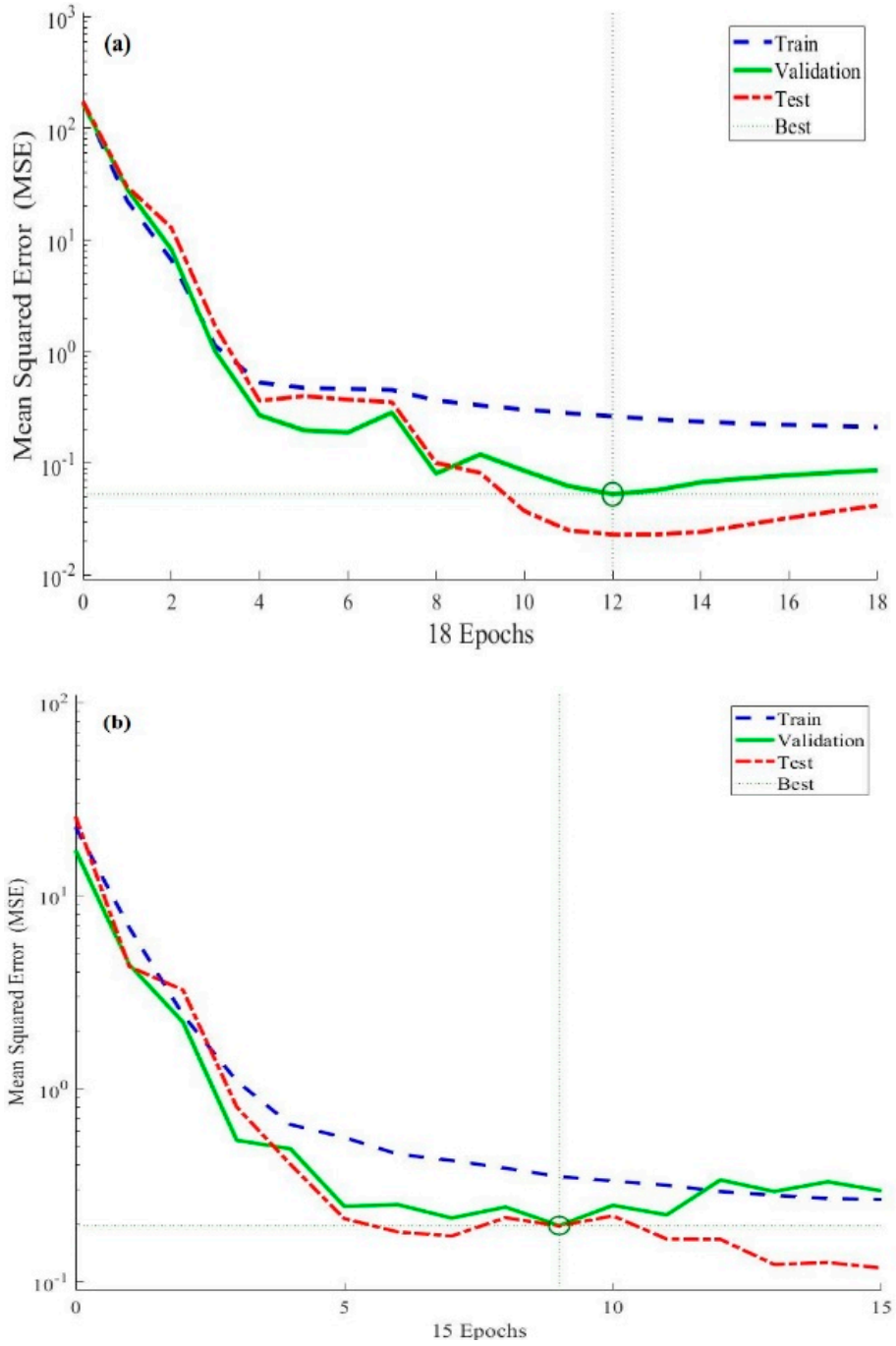

Figure 4. (**a**,**b**). The training performance graph of the ANN model for $M = 0$ and $M = 0.2$.

It is seen that the ANN model's training phases ended with the MSE values obtained for each data set meeting the most optimal position. The error histograms for the ANN model of both magnetized ($M = 0.2$) and non-magnetized ($M = 0$) flow fields are shown in Figure 5a,b. It should be observed that the calculated error rates for three different data sets

are positioned quite close to the zero-error line in the error histograms. The error levels in the error histograms are also quite low. The results of the performance and error histograms reveal that the training stages of the ANN models designed for estimating SFC values have been completed optimally.

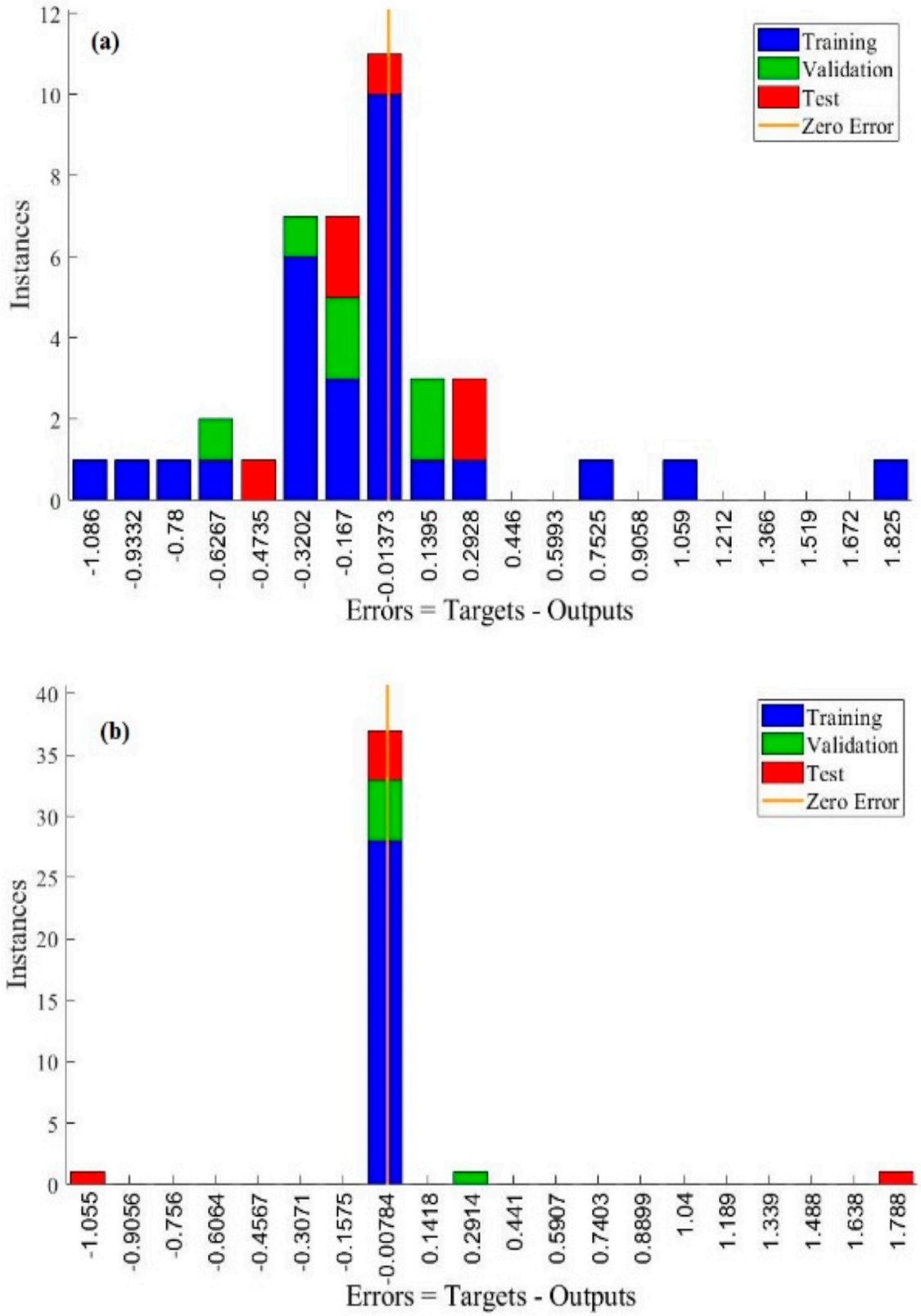

Figure 5. (**a**,**b**). Error histogram of the ANN model for $M = 0$ and $M = 0.2$.

Figure 6a,b shows the SFC values for both magnetic (M = 0.5) and non-magnetized (M = 0) flow fields, as well as the values produced using the ANN models (b).

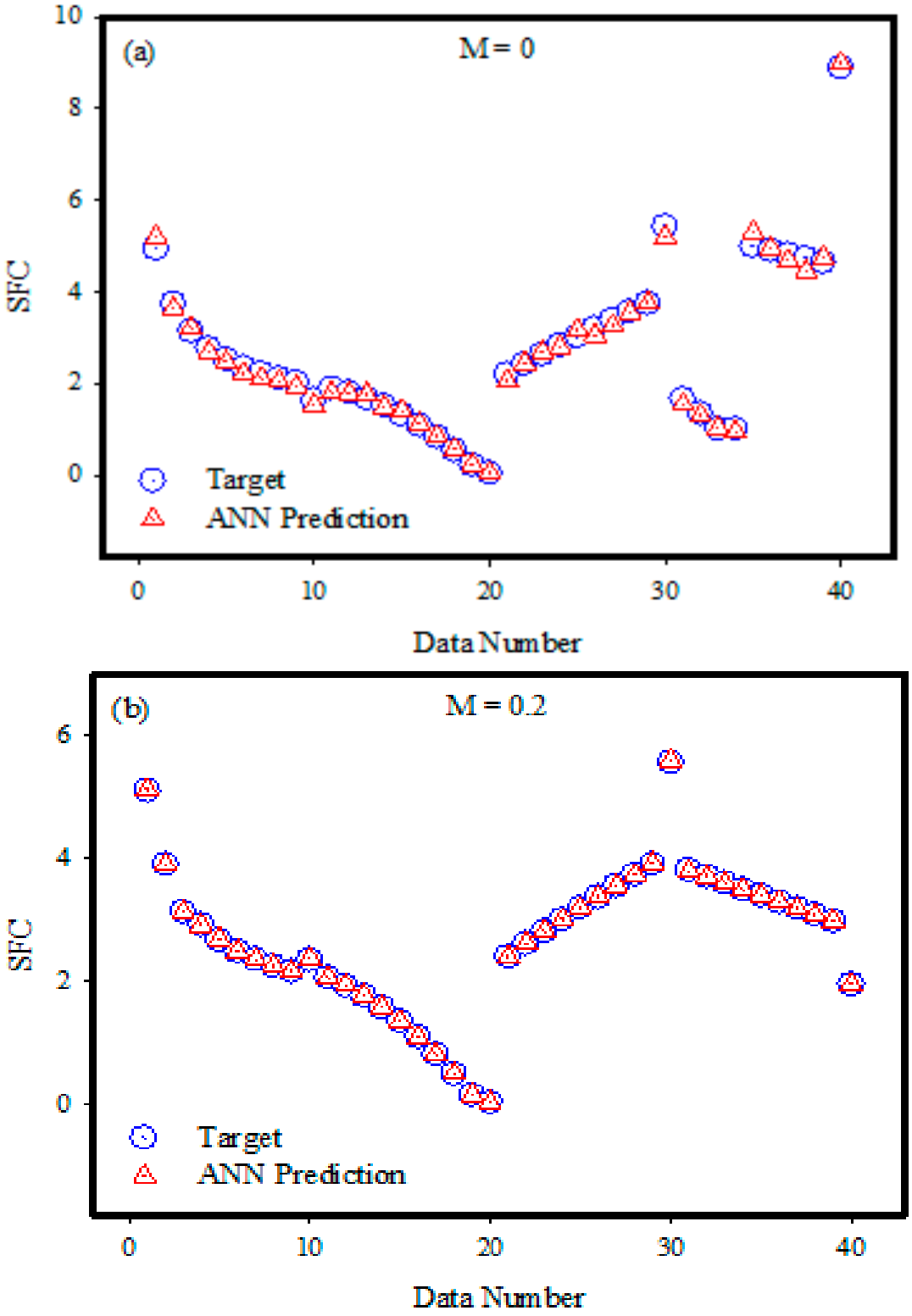

Figure 6. (**a**,**b**). The predicted and target values for M = 0 and M = 0.2.

When the outcomes for each data point are analyzed, the graphs clearly show that the ANN model results are in very good agreement with the goal values. This excellent fit

of the goal and ANN outputs demonstrates that the created ANN models can accurately anticipate SFC values.

Figure 7a,b demonstrates the deviation ratio between the SFC values derived from two different ANN models with the goal data. Such observations are completed for $M = 0$ and $M = 0.2$, respectively. Examining the MoD values obtained for each data point utilized in the creation of the ANN models reveals that the data are often concentrated around the zero-error line. The MoD data to the zero-error line indicate that the ANN outputs have low deviation rates. For a close error study of the ANN models ($M = 0$, $M = 02$), the discrepancies between the ANN model outputs and the target data are designed for the individual data points and are shown in Figure 8a,b. When the difference values for the two different ANN models are considered, it is apparent that for all of the data points, the calculated differences are quite low. The examination of the MoD and difference values reveals that both ANN models can predict SFC values with relatively low error values. The target values are on the x-axis in Figure 9a,b, and the ANN outputs are on the y-axis. When the data for two distinct ANN models ($M = 0$, $M = 02$) were reviewed, the data points were found to be quite close to the zero-error line. The numbers also show that the data points are inside the +10% error band range. Table 11 shows the performance parameters derived for two different ANN models created to estimate SFC values under different scenarios. The MoD values calculated for the ANN models are quite low, as can be observed. The low MoD values suggest that the deviation rates of the ANN model outputs are quite low. The R values' proximity to one and the low MSE values demonstrate that each ANN model can make predictions with high accuracy. The collected results suggest that each ANN model can accurately calculate the output parameter that is the SFC.

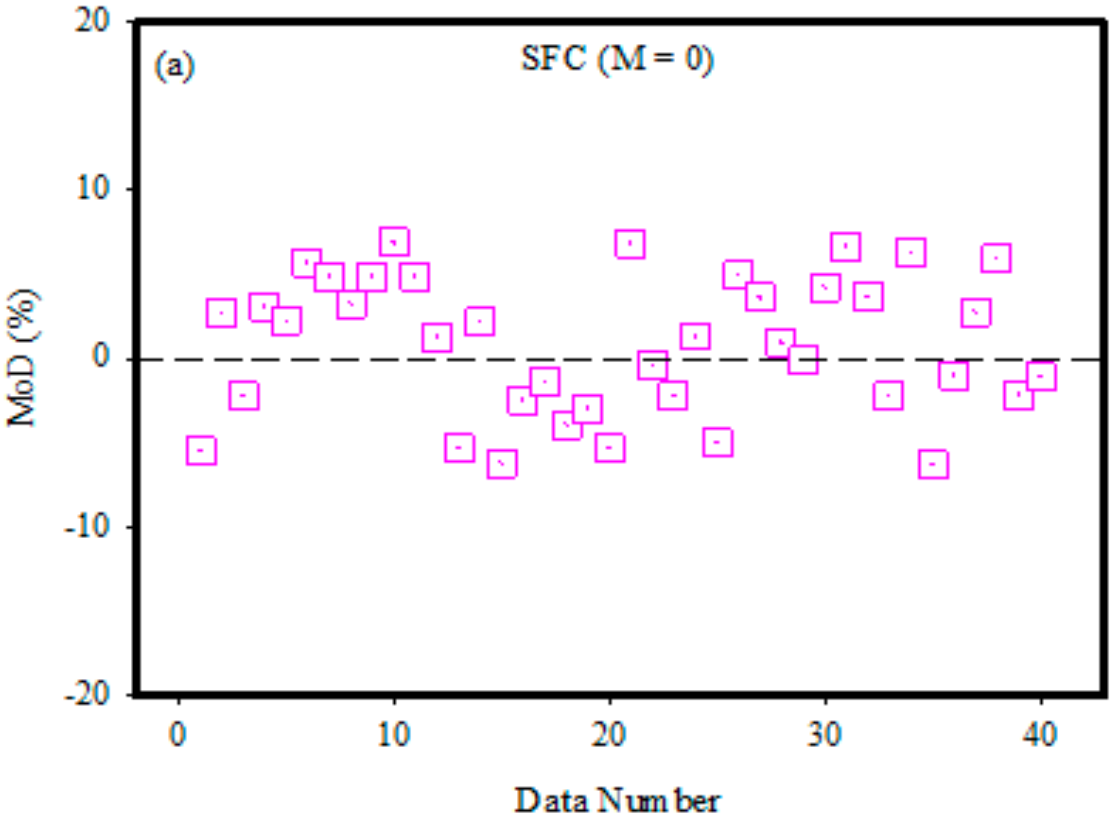

Figure 7. *Cont.*

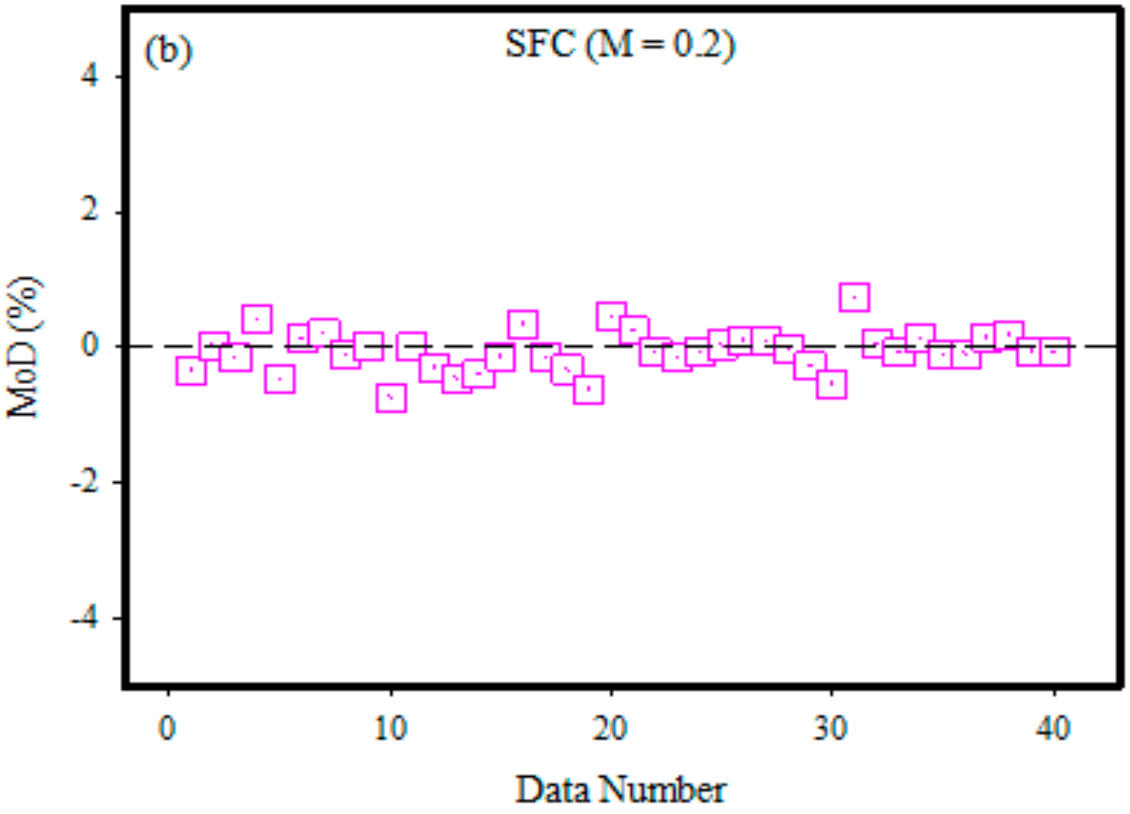

Figure 7. (**a**,**b**). MoD values for each data point for $M = 0$ and $M = 0.2$.

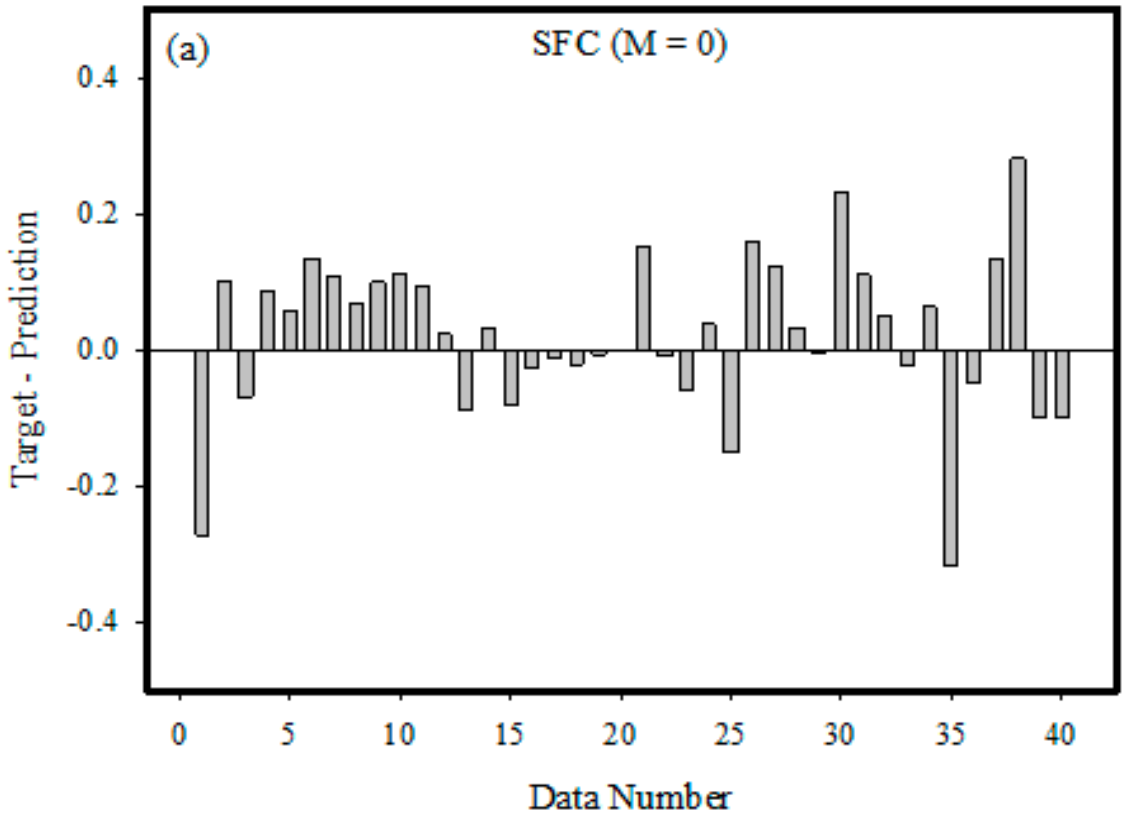

Figure 8. *Cont*.

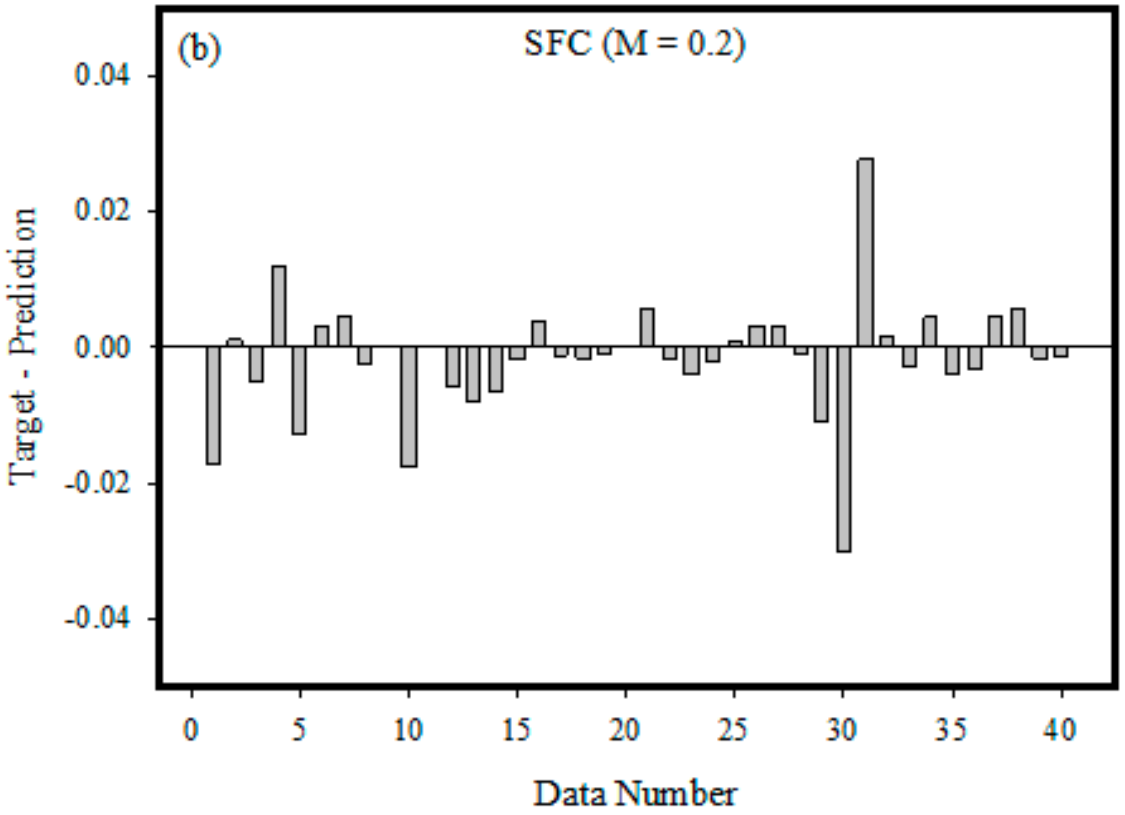

Figure 8. (**a**,**b**). The differences between the target values and the ANN outputs for each set of data when $M = 0$ and $M = 0.2$.

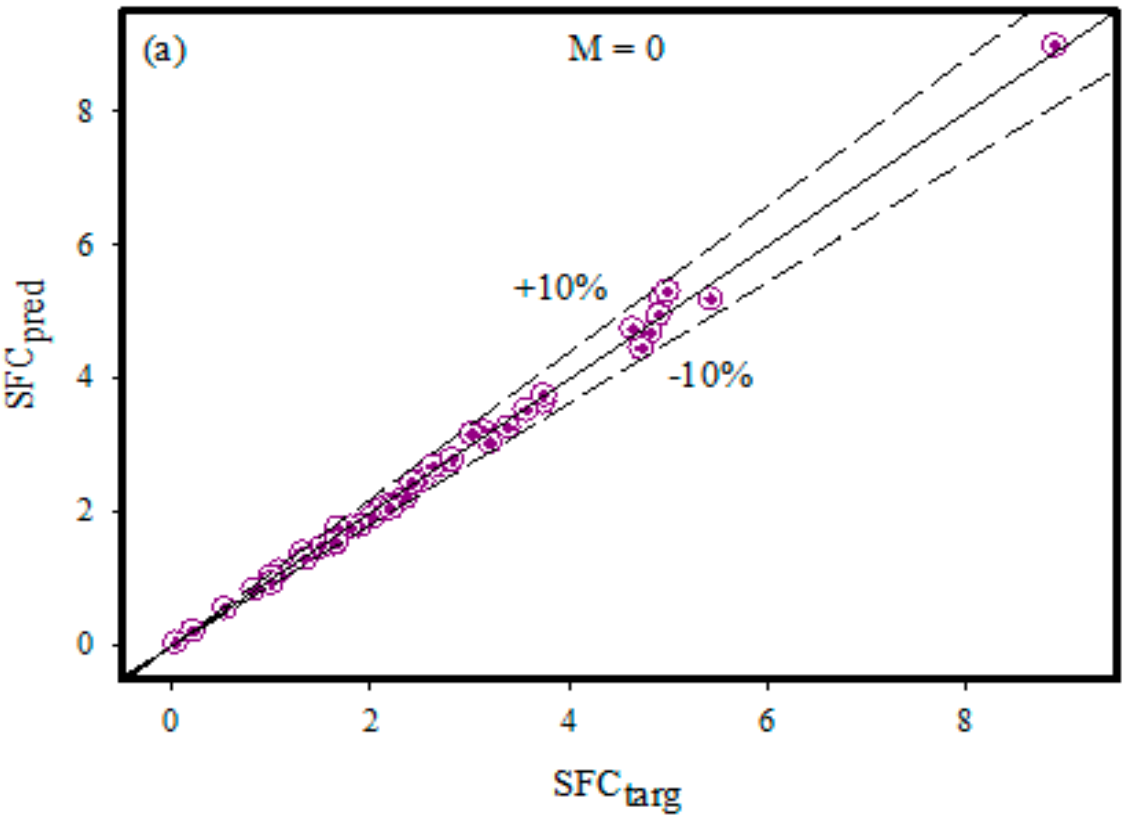

Figure 9. *Cont*.

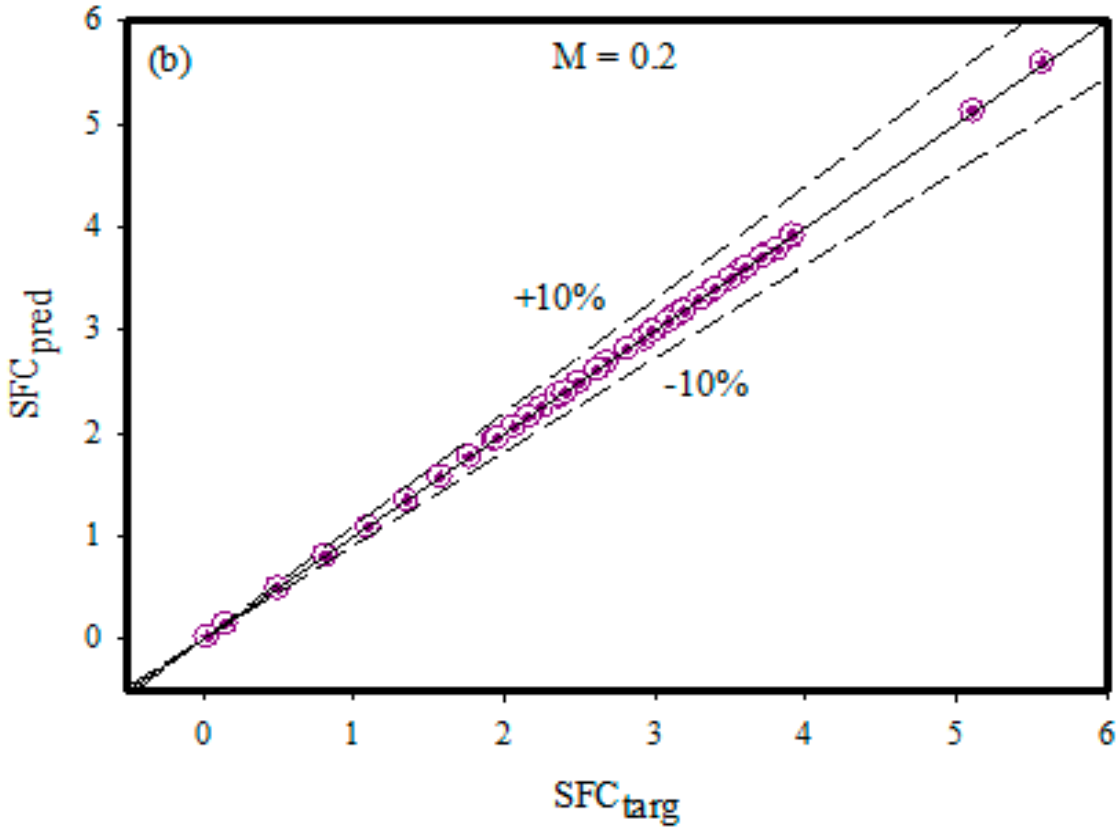

Figure 9. (**a**,**b**). Target and prediction values for $M = 0$ and $M = 0.2$.

Table 11. The performance parameters calculated for the two different ANN models.

Model	MSE	R	MoD_{min} (%)	MoD_{max} (%)
Model 1 ($M = 0$)	5.28×10^{-2}	0.96081	−0.12	6.9
Model 2 ($M = 0.2$)	2.39×10^{-5}	0.99998	0.0008	−0.74

7. Conclusions

The stagnation point flow of Casson fluid has been mathematically modelled for magnetized and non-magnetized flow fields. The novelty was enhanced by considering heat generation, viscous dissipation, mixed convection, temperature-dependent variable thermal conductivity, thermal radiations, and chemical reaction effects. The ultimate flow equations were solved by using the shooting method. The SFC values were evaluated at the cylindrical surface and the corresponding ANN models were constructed. The key outcomes are as follows:

- The margin of deviation and difference values reveals that both ANN models can predict SFC values with relatively low error values.
- The error levels in the error histograms are also quite low. Furthermore, for both ANN models, we noticed that the data points were inside the +10% error band range.
- The coefficient of determination values' proximity to one and the low mean squared error values demonstrate that each ANN model can carry out predictions with high accuracy.
- The magnitude of velocity is higher for the case of non-magnetized Casson fluid flow as compared to non-magnetic flow.
- For both chemically reactive and non-reactive flows, the concentration profiles show a declining nature towards the Schmidt number and curvature parameter.
- The SFC is found to be the decreasing function of the Casson fluid parameter and the velocities ratio parameter while the opposite is the case for the curvature parameter.

- For variation in the Casson fluid parameter, thermal Grashof number, and curvature parameter, the magnitude of SFC is higher for the case of magnetized flow as compared to the non-magnetized flow regime.

Author Contributions: Conceptualization, K.U.R. and A.B.Ç.; data curation, A.B.Ç.; formal analysis, K.U.R. and W.S.; investigation, K.U.R. and A.B.Ç.; methodology, K.U.R.; software, W.S.; Supervision, W.S. All authors have read and agreed to the published version of the manuscript.

Funding: This research received no external funding.

Institutional Review Board Statement: Not applicable.

Informed Consent Statement: Not applicable.

Data Availability Statement: The adopted methodology can be offered upon request by the readers.

Acknowledgments: The authors would like to thank Prince Sultan University, Saudi Arabia, for the technical support offered through the TAS research lab.

Conflicts of Interest: The authors declare no conflict of interest.

Nomenclature

$\widetilde{X}, \widetilde{R}$	Cylindrical coordinates
$\widetilde{U}, \widetilde{V}$	Velocity components
ν	Kinematic viscosity
β	Casson fluid parameter
β_T	Thermal expansion coefficient
g_0	Gravitational acceleration
α	Angle of inclination
β_C	Solutal expansion coefficient
$\widetilde{T}_\infty$	Ambient temperature
$\widetilde{T}$	Temperature of fluid
B_0	Magnetic field constant
$\widetilde{C}$	Concentration of fluid
$\widetilde{C}_\infty$	Ambient concentration
$\widetilde{U}_e$	Free stream velocity
σ	Fluid electrical conductivity
c_p	Specific heat at constant pressure
ρ	Fluid density
$\overline{q}$	Radiative heat flux
κ	Variable thermal conductivity
$\overline{\mu}$	Dynamic viscosity
Q_0	Heat generation coefficient
L	Characteristic length
ε	Small parameter
R_1	Radius of cylinder
k_c	Chemical reaction rate
$\widetilde{C}_w$	Surface concentration
U_0	Reference velocity
$\widetilde{T}_w$	Surface temperature
D_m	Mass diffusivity
$F_C{}'(\eta)$	Fluid velocity
$\theta_C(\eta)$	Fluid temperature
$\phi_C(\eta)$	Fluid concentration
G_T	Temperature Grashof number
G_C	Concentration Grashof number
Pr	Prandtl number
A	Velocities ratio parameter
R	Radiation parameter

γ	Curvature parameter
k^*	Coefficient of mean absorption
E	Eckert number
M	Magnetic field parameter
Rc	Chemical reaction parameter
Sc	Schmidt number
σ^*	Stefan–Boltzmann constant
H	Heat generation parameter

References

1. Alfvén, H. Existence of Electromagnetic-Hydrodynamic Waves. *Nature* **1942**, *150*, 405–406. [CrossRef]
2. Rashidi, S.; Esfahani, J.A.; Maskaniyan, M. Applications of magnetohydrodynamics in biological systems-a review on the numerical studies. *J. Magn. Magn. Mater.* **2017**, *439*, 358–372. [CrossRef]
3. Turkyilmazoglu, M. Analytical solutions to mixed convection MHD fluid flow induced by a nonlinearly deforming permeable surface. *Commun. Nonlinear Sci. Numer. Simul.* **2018**, *63*, 373–379. [CrossRef]
4. Akinshilo, A.T. Mixed convective heat transfer analysis of MHD fluid flowing through an electrically conducting and non-conducting walls of a vertical micro-channel considering radiation effect. *Appl. Therm. Eng.* **2019**, *156*, 506–513. [CrossRef]
5. Vaidya, H.; Rajashekhar, C.; Divya, B.; Manjunatha, G.; Prasad, K.; Animasaun, I. Influence of transport properties on the peristaltic MHD Jeffrey fluid flow through a porous asymmetric tapered channel. *Results Phys.* **2020**, *18*, 103295. [CrossRef]
6. Megahed, A.M.; Reddy, M.G.; Abbas, W. Modeling of MHD fluid flow over an unsteady stretching sheet with thermal radiation, variable fluid properties and heat flux. *Math. Comput. Simul.* **2021**, *185*, 583–593. [CrossRef]
7. Ali, L.; Ali, B.; Ghori, M.B. Melting effect on Cattaneo–Christov and thermal radiation features for aligned MHD nanofluid flow comprising microorganisms to leading edge: FEM approach. *Comput. Math. Appl.* **2022**, *109*, 260–269. [CrossRef]
8. Kumar, P.; Poonia, H.; Ali, L.; Areekara, S. The numerical simulation of nanoparticle size and thermal radiation with the magnetic field effect based on tangent hyperbolic nanofluid flow. *Case Stud. Therm. Eng.* **2022**, *37*, 102247. [CrossRef]
9. Casson, N. A flow equation for pigment-oil suspensions of the printing ink type. In *Rheology of Disperse Systems*; Mill, C.C., Ed.; Pergamon Press: Oxford, UK, 1959; pp. 84–104.
10. Reddy, C.; Rao, C.V.; Surender, O. Soret, Joule heating and Hall effects on free convection in a Casson fluid saturated porous medium in a vertical channel in the presence of viscous dissipation. *Procedia Eng.* **2015**, *127*, 1219–1226. [CrossRef]
11. Mohyud-Din, S.T.; Khan, S.I. Nonlinear radiation effects on squeezing flow of a Casson fluid between parallel disks. *Aerosp. Sci. Technol.* **2016**, *48*, 186–192. [CrossRef]
12. Abro, K.A.; Khan, I. Analysis of the heat and mass transfer in the MHD flow of a generalized Casson fluid in a porous space via non-integer order derivatives without a singular kernel. *Chin. J. Phys.* **2017**, *55*, 1583–1595. [CrossRef]
13. Kataria, H.; Patel, H. Heat and mass transfer in magnetohydrodynamic (MHD) Casson fluid flow past over an oscillating vertical plate embedded in porous medium with ramped wall temperature. *Propuls. Power Res.* **2018**, *7*, 257–267. [CrossRef]
14. Rehman, K.U.; Malik, M.; Zahri, M.; Tahir, M. Numerical analysis of MHD Casson Navier's slip nanofluid flow yield by rigid rotating disk. *Results Phys.* **2018**, *8*, 744–751. [CrossRef]
15. Neeraja, A.; Devi, R.R.; Devika, B.; Radhika, V.N.; Murthy, M.K. Effects of viscous dissipation and convective boundary conditions on magnetohydrodynamics flow of casson liquid over a deformable porous channel. *Results Eng.* **2019**, *4*, 100040. [CrossRef]
16. Rasool, G.; Chamkha, A.J.; Muhammad, T.; Shafiq, A.; Khan, I. Darcy-Forchheimer relation in Casson type MHD nanofluid flow over non-linear stretching surface. *Propuls. Power Res.* **2020**, *9*, 159–168. [CrossRef]
17. Farooq, U.; Hussain, M.; Ijaz, M.A.; Khan, W.A.; Farooq, F.B. Impact of non-similar modeling on Darcy-Forchheimer-Brinkman model for forced convection of Casson nano-fluid in non-Darcy porous media. *Int. Commun. Heat Mass Transf.* **2021**, *125*, 105312. [CrossRef]
18. Ramesh, G.; Roopa, G.; Rauf, A.; Shehzad, S.; Abbasi, F. Time-dependent squeezing flow of Casson-micropolar nanofluid with injection/suction and slip effects. *Int. Commun. Heat Mass Transf.* **2021**, *126*, 105470. [CrossRef]
19. Zeeshan, A.; Mehmood, O.U.; Mabood, F.; Alzahrani, F. Numerical analysis of hydromagnetic transport of Casson nanofluid over permeable linearly stretched cylinder with Arrhenius activation energy. *Int. Commun. Heat Mass Transf.* **2021**, *130*, 105736. [CrossRef]
20. Awan, A.U.; Ahammad, N.A.; Shatanawi, W.; Allahyani, S.A.; Tag-ElDin, E.M.; Abbas, N.; Ali, B. Significance of magnetic field and Darcy–Forchheimer law on dynamics of Casson-Sutterby nanofluid subject to a stretching circular cylinder. *Int. Commun. Heat Mass Transf.* **2022**, *139*, 106399. [CrossRef]
21. Gireesha, B.J.; Shankaralingappa, B.M.; Prasannakumar, B.C.; Nagaraja, B. MHD flow and melting heat transfer of dusty Casson fluid over a stretching sheet with Cattaneo–Christov heat flux model. *Int. J. Ambient. Energy* **2022**, *43*, 2931–2939. [CrossRef]
22. Rehman, K.U.; Shatanawi, W. Thermal analysis on mutual interaction of temperature stratification and solutal stratification in the presence of non-linear thermal radiations. *Case Stud. Therm. Eng.* **2022**, *35*, 102080. [CrossRef]
23. Abbas, Z.; Khaliq, S. Numerical study of non-isothermal analysis of exiting sheet thickness in the calendering of micropolar-Casson fluid. *J. Plast. Film Sheeting* **2022**, *38*, 105–129. [CrossRef]

24. Shahzad, H.; Wang, X.; Ghaffari, A.; Iqbal, K.; Hafeez, M.B.; Krawczuk, M.; Wojnicz, W. Fluid structure interaction study of non-Newtonian Casson fluid in a bifurcated channel having stenosis with elastic walls. *Sci. Rep.* **2022**, *12*, 12219. [CrossRef] [PubMed]
25. Çolak, A.B. An experimental study on the comparative analysis of the effect of the number of data on the error rates of artificial neural networks. *Int. J. Energy Res.* **2021**, *45*, 478–500. [CrossRef]
26. Güzel, T.; Çolak, A.B. Artificial intelligence approach on predicting current values of polymer interface Schottky diode based on temperature and voltage: An experimental study. *Superlattices Microstruct.* **2021**, *153*, 106864. [CrossRef]
27. Rehman, K.U.; Çolak, A.B.; Shatanawi, W. Artificial Neural Networking (ANN) Model for Drag Coefficient Optimization for Various Obstacles. *Mathematics* **2022**, *10*, 2450. [CrossRef]
28. Gedik, E.; Kurt, H.; Pala, M.; Alakour, A. An experimental and artificial neural network investigation on the laminar flow of magnetorheological fluids through circular pipes. *J. Magn. Magn. Mater.* **2022**, *546*, 168893. [CrossRef]
29. Rehman, K.U.; Çolak, A.B.; Shatanawi, W. Artificial Neural Networking (ANN) Model for Convective Heat Transfer in Thermally Magnetized Multiple Flow Regimes with Temperature Stratification Effects. *Mathematics* **2022**, *10*, 2394. [CrossRef]
30. Srinivasacharya, D.; Kumar, R.S. Artificial neural network modeling of the Casson fluid flow over unsteady radially stretching sheet with Soret and Dufour effects. *J. Therm. Anal. Calorim.* **2022**, *147*, 14891–14903. [CrossRef]